PhotoniX

RESEARCH Open Access

Real-time monitoring of fast gas dynamics with a single-molecule resolution by frequency-comb-referenced plasmonic phase spectroscopy

Duy-Anh Nguyen[1,2†], Dae Hee Kim[1†], Geon Ho Lee[1], San Kim[3,4], Dong-Chel Shin[1], Jongkyoon Park[3,4], Hak-Jong Choi[6], Seung-Woo Kim[1], Seungchul Kim[3,4*] and Young-Jin Kim[1,5*]

[†]Duy-Anh Nguyen and Dae Hee Kim contributed equally.

*Correspondence: s.kim@pusan.ac.kr; yj.kim@kaist.ac.kr

[1] Department of Mechanical Engineering, Korea Advanced Institute of Science and Technology (KAIST), Science Town, Daejeon 34141, South Korea
[3] Department of Cogno-Mechatronics Engineering, College of Nanoscience and Nanotechnology, Pusan National University, Busan 46241, South Korea
Full list of author information is available at the end of the article

Abstract

Surface plasmon resonance (SPR) sensors are based on photon-excited surface charge density oscillations confined at metal-dielectric interfaces, which makes them highly sensitive to biological or chemical molecular bindings to functional metallic surfaces. Metal nanostructures further concentrate surface plasmons into a smaller area than the diffraction limit, thus strengthening photon-sample interactions. However, plasmonic sensors based on intensity detection provide limited resolution with long acquisition time owing to their high vulnerability to environmental and instrumental noises. Here, we demonstrate fast and precise detection of noble gas dynamics at single molecular resolution via frequency-comb-referenced plasmonic phase spectroscopy. The photon-sample interaction was enhanced by a factor of 3,852 than the physical sample thickness owing to plasmon resonance and thermophoresis-assisted optical confinement effects. By utilizing a sharp plasmonic phase slope and a high heterodyne information carrier, a small atomic-density modulation was clearly resolved at 5 Hz with a resolution of 0.06 Ar atoms per nano-hole (in 10^{-11} RIU) in Allan deviation at 0.2 s; a faster motion up to 200 Hz was clearly resolved. This fast and precise sensing technique can enable the in-depth analysis of fast fluid dynamics with the utmost resolution for a better understanding of biomedical, chemical, and physical events and interactions.

Keywords: Frequency comb, Nanohole array, Single molecule detection, Refractive index, High resolution, High speed, Traceability to time standard

Individual quantum-resolution detection is the ultimate goal of all sensors, which has motivated extensive research on monitoring of gas or liquid dynamics at a single-molecule resolution to understand their fast chemical and biological interactions in microenvironments [1]. Furthermore, the detection must be sufficiently fast to monitor the association events, because the event time of bio- and chemical-interactions (e.g. ligand binding) in a high-affinity solution ranges from sub-second to several minutes for nanomolar and micromolar complexes [2]. Meanwhile, wide-field measurements have

also evolved unceasingly, where multiple single-molecule-resolution detections have been accomplished in parallel, enabling a higher-throughput detection [3]. To meet these requirements, optical methods are considered the most suitable owing to their high sensitivity, high-speed photon-sample interaction, environmental robustness, and electrical passiveness. Successful demonstrations have been performed in fluorescence microscopy [4, 5], surface-enhanced Raman spectroscopy (SERS) [6–8], single-molecule localization microscopy [9], human disease diagnostics [10], DNA sequencing [11], enzyme-linked immunosorbent assay [12], and molecular biology [13]. Regarding the state-of-the-art detection limits, the liquid-phase sensing supports a detection resolution of 2.0-nM at a laser focal volume of 10^{-15} L after the dilution [3], while the gas-phase sensing does a concentration of 1.0 part-per-billion (ppb, 10^{-9}) [14, 15], which is limited by the thermal noise [16]. These single-molecule level detections have been realized only at extremely low concentration environments with strong dilution over a long observation time. However, there has been an increase in demand for extreme sensitivities under significantly higher concentration (~ μM) with shorter lifetime coverage of a few seconds or less, which cannot be accomplished with existing state-of-the-art technologies [2]. Stronger photon-matter interaction is the prerequisite for realizing higher resolution, higher speed detection over a parallelized platform.

Surface plasmons are coherent charge oscillations produced by the strong resonant interaction of photons and free electrons at the interface of metallic and dielectric materials [17, 18]. Surface plasmon resonance (SPR) sensors with metal thin-films have improved the sensitivity of traditional Raman and fluorescence spectroscopy by 2 ~ 3 orders of magnitudes [19, 20], while increasing the excitation and emission rates of the Raman signals up to 10 orders of magnitudes [21]. Compared to traditional SPR sensors based on metal thin-films, nano-engineered SPR sensors can reduce the footprint of a unit probe; therefore, they support smaller observation volumes, essential for single molecular level detection at high concentrations. A single sensor unit can contain numerous nanoscale detection probes, which enables wide-field measurement. Moreover, the nanostructures provide an additional interesting possibility, that is, the optical trapping of target molecules including thermo-phoresis and thermo-osmosis [22]. General optical trapping utilizes photon energy to trap an object at the focal volume of the laser beam [23]; this force, including the scattering and gradient forces, is generally small, and thus, has a clear effect on the particles with a size ranging from tens of nanometers to micrometers [24]. In the Rayleigh regime, where the particles size is smaller than the light wavelength, the gradient and scattering forces are proportional to the third and sixth power of the particle radius, respectively [25]. Therefore, gas molecules with Van der Waals radius of hundreds of picometers can easily escape from the trap due to their Brownian motions [26]. Interestingly, intense local field gradients in the vicinity of metal nanostructures have been revealed to support optical-field-induced molecular trapping, for the molecules in solutions; however, that has not been demonstrated for the gaseous constituents. Apart from the radiative scattering, the light absorbed by the metal nanostructures can be relaxed in a non-radiative way and induce strong heat energy around the nanostructures owing to the ohmic loss. This phenomenon can lead to the optical thermal effect, which can manipulate and transport even smaller sub-10 nm objects via plasmon-induced thermal convection. This is referred to as thermo-phoresis, which

functions on top of the plasmonic nanohole array [27]. Therefore, this thermophoretic force can be a potential workforce candidate for gaseous targets as an efficient plasmonic trapping mechanism, although no demonstration has been exhibited to date.

Most plasmonic sensors are based on intensity interrogation [28, 29] and support a resolution of ~ 10^{-6} RIU (RIU: Refractive Index Unit) [30–32], while being limited by environmental and instrumental noises (see Figure S1, Table S1 in Supplementary Section A). The plasmonic phase can provide much more abundant information about the sample than the intensity; however, high-resolution detection of the optical phase has remained difficult owing to the low wavelength stability of available light sources. Certain early research works have proven the potential by exhibiting a 1,000-fold improvement in the detection sensitivity, 10^{-8} RIU [32, 33], with the concentration of 10^{-4} pg $mm^{-2,}$ [34], or pM [35]. Most phase studies have used interferometric ellipsometers [33–35], where the polarization-dependent phase difference is detected by mechanically rotating polarizing optics, limiting the detection speed to the second to minute timescale. The authors recently reported a fast and precise plasmonic ruler by introducing heterodyne phase detection. Our Mach–Zehnder interferometer utilizes heterodyne detection with a frequency-shifted reference beam, enabling detection speeds orders of magnitude faster, limited only by the photodetector and digitizer bandwidth. This technique can measure phase changes at high speeds, typically in the range of kilohertz, using a frequency comb as a new class of wavelength-stable light source for plasmonic phase monitoring [36]. The frequency comb provides millions of well-defined optical modes over a broad spectrum with a high phase coherence referenced to an atomic clock of a time standard [37–39]. The use of such a frequency comb has resulted in remarkable advances in high-resolution atomic/molecular spectroscopy, the broadband calibration of astronomical spectrographs, time/frequency transfer over long distances, absolute laser ranging, and the inter-comparison of atomic clocks [40–43]. The frequency comb's wide spectral coverage allows simultaneous selection of an off-resonance reference wavelength and an on-resonance signal wavelength, which is crucial for our differential phase detection scheme and challenging to achieve with a single-wavelength tunable laser. The interrelationship between the frequency comb and surface plasmons was first reported by the authors, where superior performance of the frequency comb could be maintained with negligible degradations in absolute frequency position, stability and linewidth [44]. These performances were utilized to realize picometer resolution in real-time monitoring of physical motions of the plasmonic sample [36]. However, demonstrations on monitoring of fast and precise fluidic motions, for a better understanding of atomic or molecular dynamics, are yet to be performed.

Here, we demonstrate fast and precise detection of gaseous atomic dynamics at single-molecule resolution per plasmonic structure using frequency-comb-referenced (FCR) plasmonic phase spectroscopy. The photon-sample interaction was enhanced by a factor of 3,852 more owing to strong plasmonic resonance and optical trapping effect via thermophoresis than the same physical sample thickness. By utilizing a sharp plasmonic phase resonance and a high heterodyne information carrier of 36.2 MHz, a small dynamic atomic density modulation with an amplitude of 11.2 atoms per nanohole was clearly resolved at 5 Hz with a resolution of 0.06 atoms per nanohole in Allan deviation. Furthermore, the use of hundreds of unit nanostructures

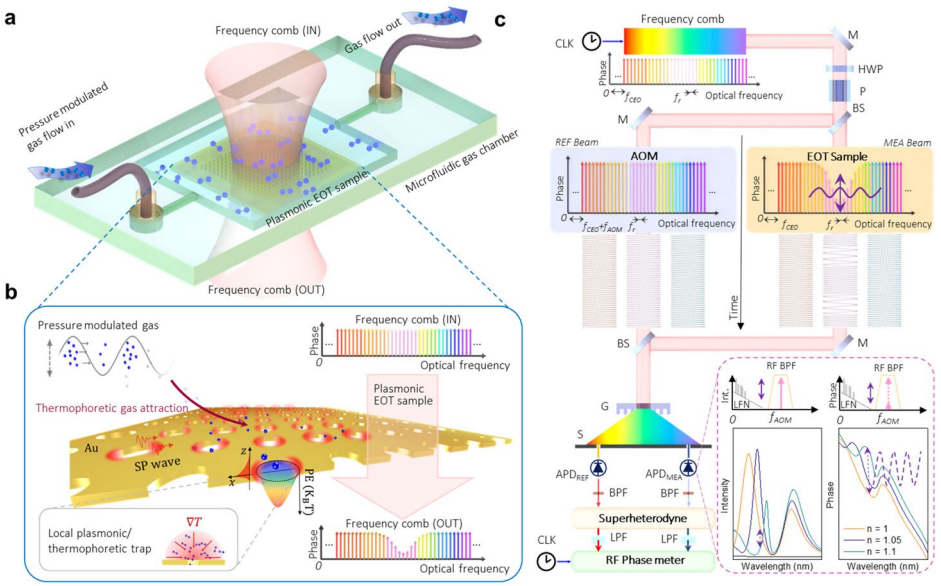

Fig. 1 Frequency-comb-referenced plasmonic phase spectroscopy for gas sensing. **a** The frequency comb excites the free charge on the Au surface which generates the surface plasmon wave traveling at the interface of the metallic and gas layer. The gaseous atomic/molecular density change by the pressure modulation on the surface contributes to the plasmonic phase change of the transmitted frequency comb. The gas chamber has an inlet and outlet for the continuous gas supply. The sample was attached on one side of the chamber. **b** The gas pressure was modulated at a specific frequency as the gas flows through the chamber. The gas atoms/molecules are gently directed toward the surface of the nanohole array by the thermophoretic force; then, the plasmonic field around the nanohole traps the gas atoms/molecules. **c** principle of phase spectroscopy. It is based on the Mach–Zehnder interferometer, in which the measuring and frequency-shifted reference beams interfere to generate heterodyne beat signals. The signals were detected using a photodetector. The relative phase was obtained through a comparison to the reference signal using a high-resolution phase meter referenced to an atomic clock. Consequently, when a small oscillation of the gas pressure is applied, the FCR phase spectroscopy can detect gaseous atomic/molecular modulations with a single-molecule resolution at an update rate of hundreds of hertz. Beam splitter (BS), polarizer (P), lens (L), mirrors (M), avalanche photodetectors (APD), gratings (G) and splits (S)

increased the effective surface area per unit mass, resulting in a significant increase in the photon-matter interaction probability, thereby improving the measurement speed. Consequently, dynamic fluidic modulations at the frequency up to 200 Hz was successfully detected. Such fast and precise sensing principle can enable the in-depth analysis of fast fluid dynamics with the utmost single-molecule resolution. By introducing chemical selectivity via functionalizing the plasmonic sample surfaces with bio-receptors, such as aptamers or bacteriophages, real-time detection of respiratory viruses (e.g. COVID-19) could be realized without time-consuming polymerase chain reaction (PCR) [45–47].

The basic concept and optical configuration of frequency-comb referenced (FCR) plasmonic phase spectroscopy for gas sensing is illustrated in Fig. 1. The gas atoms/molecules travel over the plasmonic sample located in a microfluidic chamber (see Fig. 1a). First, the frequency comb excites the free charges on the Au surface, which generates a surface plasmon (SP) wave traveling at the interface of the metallic and gas layers (see Fig. 1b). Then, SPs are guided through the nanohole and reverted to photon. During this process, the plasmonic coupling and interference among the multiple waves in the nanohole array result in extraordinary optical transmission (EOT), which significantly

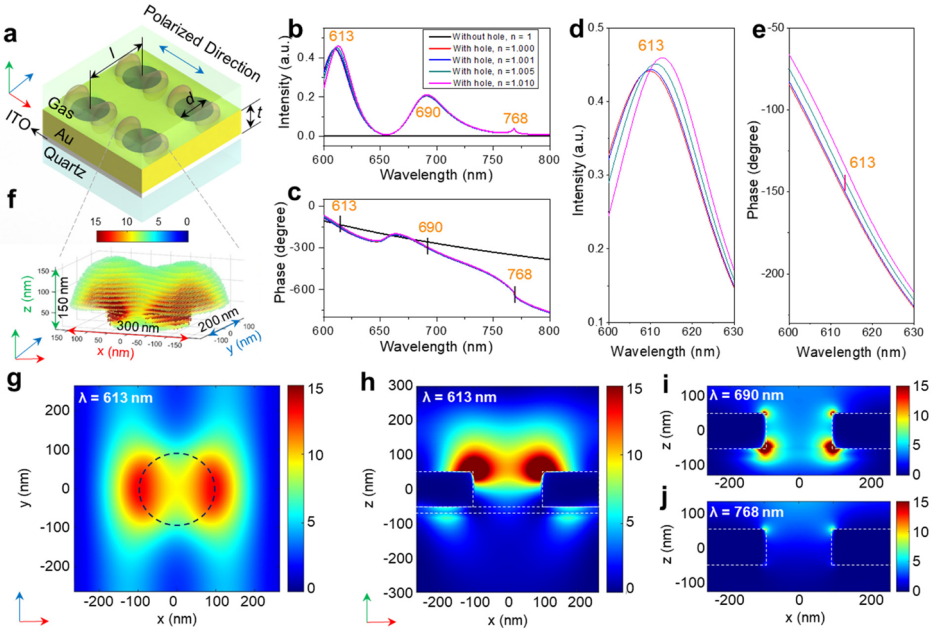

Fig. 2 Plasmonic sample model in FDTD simulation. **a** Plasmonic sample structure with three geometric parameters, pitch (l), hole diameter (d), and Au film thickness (t) were optimized to 530, 200, and 100 nm, respectively, on a 25-nm-thick ITO-coated quartz substrate. **b** Transmission intensity for different gas refractive indices. **c**, spectral phase change for various gas refractive indices. **d**,**e** Amplified view at the wavelength of interesting– 613 nm, where the change in both intensity and phase are strongest. **f** 3D view of the calculated intensity distribution $|E|^2$ ($\lambda = 613$ nm) around a nanohole. **g** Calculated intensity distribution at 50 nm above from the Au surface ($\lambda = 613$ nm). **h**,**i**,**j** Calculated intensity distribution around a plasmonic nanohole taken at the side at wavelengths of 613, 690, and 768 nm, respectively

enhances the transmission of light. Simultaneously, the traveling gas atoms/molecules are first gently directed toward the surface of the nanohole array due to the thermophoretic force; this force is induced by nanohole array, not the individual nanohole. Then, the plasmonic field of each nanohole attracts the atoms/molecules closer to the nanoholes and traps them. This unique combination of optical confinement effects permits the significantly stronger interaction between the SP wave and gas atoms/molecules at the gas-metal interface, which results in the drastic spectral phase changes that are essential for high resolution gas detection. The frequency-comb-referenced (FCR) heterodyne laser interferometry extracts the phase information of this EOT transmission (see Fig. 1c, see further details in Methods), where the frequency comb was wavelength-stabilized to a rubidium atomic clock of a time/frequency standard. To minimize the environmental noise, this interferometer is devised based on common-path configuration with differential phase detection scheme, where the reference and measurement beams travel the same path length with different wavelengths. The measurement beam passes through the plasmonic sample while the reference beam is frequency-shifted by the acousto-optic modulator to generate the heterodyne beat frequency at 40 MHz. The reference beam wavelength is carefully chosen to be far from the plasmonic resonance peak, where the sample's influence on the transmitted light phase is minimal (see Fig. 2). This ensures that any phase changes induced by the sample on the reference beam are negligible compared to the large phase changes experienced by the signal beam at the

resonance wavelength. Because the resulting signal is at high radio-frequency (RF) regime by a pair of photo-detectors, low-frequency environmental noise could be suppressed via RF band-pass filtering. Further, the differential phase was determined with a high-resolution phase meter with an update rate of 1.0 kHz referenced to a Rb atomic clock. This series of laser wavelength stabilization, common-path differential interferometer configuration, and RF heterodyne detection with noise rejection filtering, resulted in the successful detection of fast gaseous atomic/molecular dynamics with a single-molecule resolution at a high update rate of hundreds of hertz.

The plasmonic EOT sample was designed and optimized to be resonant with the frequency comb by solving Maxwell equations using a finite-difference time-domain (FDTD) (see Fig. 2). The structure was designed to have a maximum optical transmittance at the spectral range of the frequency comb over 600–850 nm (see Fig. 2a-c). When the wavelength of the incident light matched with the resonant peak of the plasmonic EOT sample (see Fig. 2b-d), the sample strongly absorbed the light such that the electric fields became highly localized in the vicinity of the sample (see Fig. 2f-j). Meanwhile, strong resonance changes can be observed at the plasmonic phase as well as the transmitted intensity because the phase is proportional to the first derivative of the intensity spectrum. Therefore, the phase detection is known to be much more sensitive to the sample changes (see Fig. 2c and e). Three geometric parameters, pitch (l), hole diameter (d), and Au film thickness (t) (see Fig. 2a) were optimized to 530, 200, and 100 nm, respectively, by FDTD simulation. The transmitted intensity and phase spectrum for different gas refractive indices were obtained as shown in Fig. 2b to e. the horizontal intensity peak shifts (see Fig. 2b) can be observed clearly and the vertical phase differences (see Fig. 2c, d, e) are strongest at the 613 nm peak compared to the other resonance positions (at 690 and 768 nm). Because the metallic surface is in contact with two media (substrate glass and gas over the plasmonic structure), two groups of resonance were observed [48]. This can be explained by analyzing the electric field distribution at the gas and metallic interface from the side view (see Fig. 2h, i, and j), which is the strongest in the gas at 613 nm and reduces drastically at 690 and 768 nm with different enhancement positions. The enhanced electric field was distributed over a volume of $300 \times 200 \times 150$ nm^3 (length $\times$ width $\times$ height) (see Fig. 2f, g, h) with the same polarization direction as the incident light. Hence, the effective observation volume was 9.0 attoliters, that is, three orders of magnitudes smaller than the optical diffraction limit. This space is the main interaction volume of the SP and gaseous target atoms/molecules. To avoid the potential geometrical deflection due to pressure or electrostatic attraction, a plasmonic resonance mode at 613 nm was carefully chosen to prioritize photon-fluid interaction with minimal impact from physical motions (see Figure S2 in Supplementary Section B). By securing the sample to the substrate using epoxy glue, minimal mechanical deflection was ensured while maintaining heat conduction, enabling high-resolution gas concentration measurements in the control experiments.

The first set of experiments was conducted to estimate the sensitivity enhancement factor of the proposed FCR phase spectroscopy as shown in Fig. 3a. Figure 3a presents the microfluidic gas chamber with a periodic gas density modulation apparatus. One chamber was setup without the sample as the control reference while the other chamber enclosed an EOT sample with a chamber height of 300 μm. The flow pressure of the

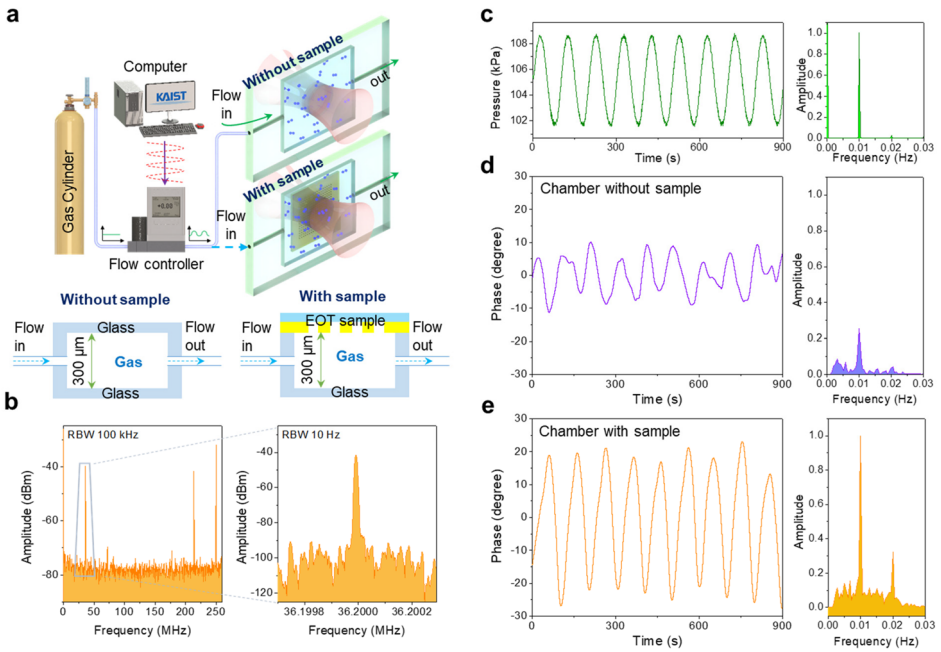

Fig. 3 Plasmonic phase spectroscopy with gas pressure control. **a** The microfluidic gas chamber with a periodic gas density modulation apparatus. One chamber was set up without the sample as the control reference while the other chamber enclosed an EOT sample with a chamber height of 300 μm. **b** The measured heterodyne RF beat spectra with a signal-to-noise ratio of ~ 40 dB at resolution bandwidth of 10 Hz. **c** Pressure variation measured by a sensor inside the flow controller. The Fourier transformed frequency spectrum (right) shows a clear peak at 0.01 Hz. **d** The measured phase modulation in the case of the chamber has no EOT sample (left) and its Fourier transform (right) of the case "chamber without EOT sample. **e** The measured phase (left) and its Fourier transform (right) of the case "chamber with EOT sample". Comparing **d** and **e** the EOT shows it has advanced ability in gas sensing

noble Ar gas was periodically modulated with an amplitude of 6.89 kPa at a frequency of 0.01 Hz using a flow controller (see Fig. 3c), which corresponded to a refractive index change of 1.7×10^{-5} RIU inside the chamber (see Table S2, Table S3 in Supplementary Section C). The plasmonic phase response of the transmitted light was detected using a common-path heterodyne differential interferometer. Figure 3b shows the measured heterodyne RF beat spectra with a signal-to-noise ratio of ~ 40 dB at resolution bandwidth of 10 Hz. First, the phase response of the reference chamber without the EOT sample was analyzed as shown in Fig. 3d. The gas pressure modulation could be resolved via phase at the modulation frequency of 0.01 Hz with an amplitude of 10.2°. This phase change was achieved by the physical refractive index change induced by the gas pressure modulation without the plasmonic resonance effects; therefore, the phase modulation was unclear and dominated by the environmental noise. Second, the phase response of the other chamber with the plasmonic EOT sample was examined. A clear phase modulation was observed at the same frequency of 0.01 Hz with 4.15 times stronger modulation amplitude of 42.3° than the reference chamber case. The simple insertion of the plasmonic EOT sample with a negligible volume change facilitated the attainment of an additional phase sensitivity 32.1° via the plasmonic effects. Further, the plasmonic enhancement factor was determined by considering the phase changes per the unit observation volume at the cases with and without the EOT sample. The observation

volume encompasses the volume of the enhanced electric field surrounding the nanohole and the hole volume (see Fig. 2f). When dividing the phase addition for the EOT sample of 32.1° by the increased effective thickness of 250 nm (the addition of 150 nm of plasmon-enhanced field height and 100-nm thick Au layer of the EOT sample), the plasmonic enhancement factor was determined to be 3,852; this implies that the phase shift in this measurement was 3,852 times larger than the expected RI change in same physical volume without EOT sample under the same gas modulation. Surprisingly, this is also 506 times higher than that estimated by FDTD simulation (see Fig. 2e). This implies that the interaction of light with the nanohole array is not simply determined by the EOT but is also governed by additional mechanisms, such as optical trapping, electrophoresis, dielectrophoresis, electrostatic attraction, and the Casimir-Polder effect. However, these forces have minor effects on smaller molecules, like Argon gas in this research; the major force in this regime is thermophoresis, which does not depend on the size of the molecules together with plasmonic trapping around the nanostructures (see Table S4 in Supplementary Section D); plasmonic trapping effects were recently reported in Refs. [24, 49, 50].

The thermophoresis creates local fluidic convection around the sub-wavelength hole [51–53] and quenches the Brownian motion of trapped molecules [49, 54]. Consequently, they bend the gas flow toward the Au surface and increases the local refractive index around a nanohole. To explore the possible contribution of thermophoresis, simulations and experiments were conducted as shown in Fig. 4. The strength of the thermophoresis is known to be dependent on the laser power and flow speed, thus, the phase was measured with different input power and flow speed. For more detailed understanding, the AC electric field was introduced in addition as shown in Fig. 4a; this platform enables us to verify whether the phase enhancement is supported by the thermophoretic force or not. If the thermophoretic force is involved in our phase detection, the total force $\mathbf{F}(\mathbf{r})$ with the AC field can be described as a function of temperature gradient, $\nabla T(\mathbf{r})$ around the nanostructure together with the secondary gradients in permittivity (ε) and electrical conductivity (σ) of the fluid, which can be described by

$$\mathbf{F}(\mathbf{r}) = \frac{1}{2} Re\left[\frac{\varepsilon(\alpha - \beta)}{1 + i\omega\tau}(\nabla T(\mathbf{r}) \bullet \mathbf{E})\mathbf{E}^* - \frac{1}{2}\varepsilon\alpha|\mathbf{E}|^2\nabla T(\mathbf{r})\right] \quad (1)$$

where $\alpha = (1/\varepsilon)(\delta\varepsilon/\delta T)$, $\beta = (1/\sigma)(\delta\sigma/\delta T)$, $\tau = \varepsilon/\sigma$, ω is the angular frequency of AC electric field ($\mathbf{E}$) [51]. Then, the flow bending effect of thermophoresis can be manipulated by controlling AC electric field, as shown in Fig. 4b. The AC electric field (20 MHz) was applied to the plasmonic sample by connecting the AC source with the Au side of the sample and ITO-coated glass (transparency: 78.8%, sheet resistance: 5.4–6.8 Ω/sq), with a gap of 100 μm. The plasmonic sample was illuminated by a 100-mW broadband frequency comb (600–850 nm). Because the laser beam was incident on the quartz substrate side, the contribution of the optical trapping effect caused by the focus point could be ignored. Under this condition, the temperature distribution around the nanoholes was simulated as shown in Fig. 4c; the temperature around the nanoholes was higher by 12 °C. This temperature difference generates local fluid flow that attracts the gas to the sample side as shown in Fig. 4d, e (see Methods for the details). As the flow speed gradually increases from 0 to 10 μm/s, the contribution of the local convection became

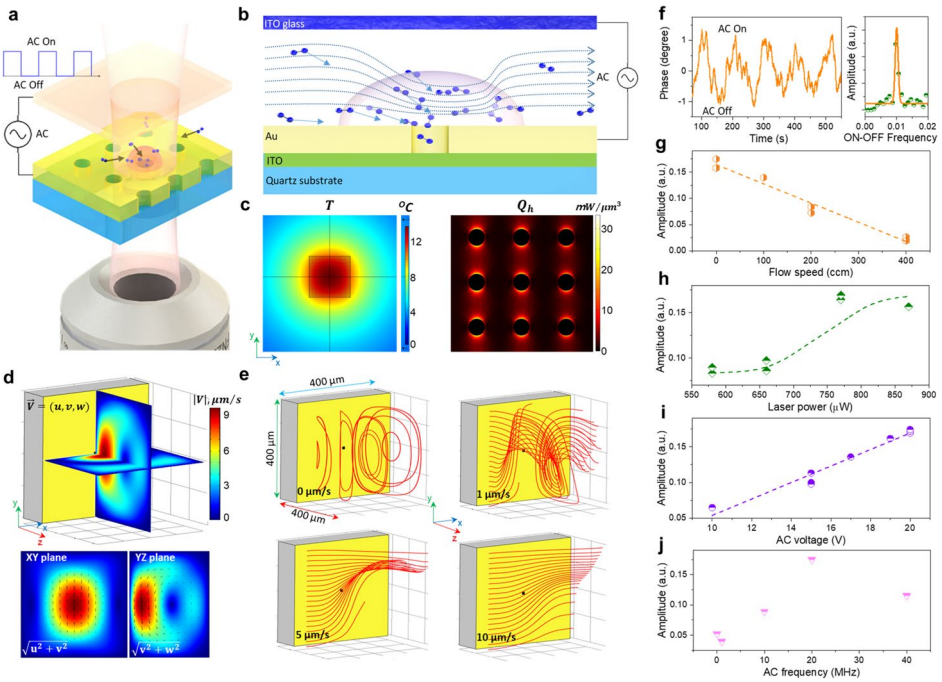

Fig. 4 Thermophoresis demonstration. **a** Schematic of the experiment b EOT sample when an AC field is applied. The AC source was connected to the Au layer of the plasmonic sample and ITO glass above the sample. AC field could enhance the thermophoresis effect, which directs the gas flow toward the Au surface. **c** Numerical simulations of the temperature increase (***T***) and heat source density (***Q***) of a nanohole array. **d** Fluid simulation with the appearance of the temperature gradient with a gas flow speed of 0 µm/s. **e** Streamlines simulation with different gas flow speeds of 0, 1, 5, and 10 µm/s. **f** The phase response when the AC field was turned ON and OFF with a specific frequency (left) and its Fourier transform (right). **g** The Fourier-transformed amplitude of the measured phase with different gas flow speeds. The dashed line represents an exponential decay fit to the data, indicating the decrease in thermophoretic force with increasing flow speed. **h** The Fourier-transformed amplitude of the measured phase with different input optical powers. The dashed line represents a nonlinear fit to the data, consistent with the thermophoretic force being proportional to the temperature gradient induced by the optical power. **i** The Fourier-transformed amplitude of the measured phase with different AC voltages. The dashed line represents a linear fit to the data, confirming the linear relationship between the thermophoretic force and the applied AC electric field. **j** The Fourier-transformed amplitude of the measured phase with different AC frequencies

less significant (see Fig. 4e). When the AC field was periodically turned on and off with a frequency of 0.01 Hz, the phase modulation was clearly resolved in both the time and frequency domain, as shown in Fig. 4f. As the flow speed increases from 0 to 400 ccm, the amplitude of the Fourier-transformed frequency peak (Fig. 4f inset) was gradually reduced and disappeared when the speed up to 400 ccm, as shown in Fig. 4g; this flow speed covers the flow state changes from steady to laminar and turbulent flows. This result is consistent with the simulation performed using COMSOL Multiphysics software (Fig. 4e, see Figure S4 in Supplementary Section G). Further, thermophoresis was also confirmed to be dependent on the input optical power as demonstrated in Fig. 4h. The higher input power supports a stronger temperature gradient resulting in a stronger gas confinement effect; the green trendline shows non-linear relationship between them, which matches well with Eq. 1. Meanwhile, the frequency peak amplitude (in Fig. 4f right panel) changes proportionally to the AC field as shown in Fig. 4i. Because all the other components in Eq. (1) remain the same except for the input electric field,

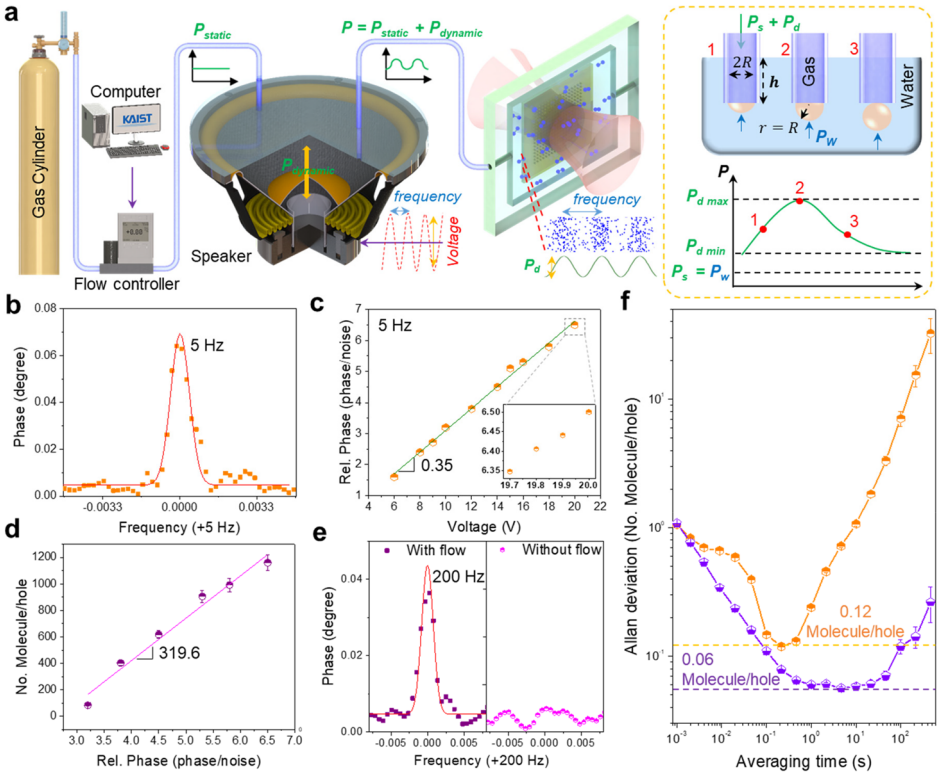

Fig. 5 High resolution and high-speed measurement. **a** The Pascal level pressure modulation applied to gas flow using a speaker. The gas flow with a constant value controlled by the flow controller goes through the speaker to bring out the pressure generated by the speaker. To change the frequency and amplitude of the pressure, the speaker was controlled using a frequency generator. The sound propagation changes the pressure inside the chamber at Pascal levels. The pressure was measured using the maximum bubble pressure method (the inset) **b** Phase change at the modulation of 5 Hz with the gas flow and Gaussian fitting. **c** Relation between the speaker-controlled voltage and relative phase (peak intensity/noise level) at 5 Hz. **d** Relation between the relative phase and level of molecule modulation. **f** Resolution analysis using Allan deviation. Compared to FCR non-differential plasmonic phase spectroscopy, FCR differential plasmonic phase spectroscopy provides two times better stability. **e** Phase change at the modulation of 200 Hz in the presence (left) and absence (right) of gas flow

E, F(r) is proportional to $|E|^2$. The AC frequency was optimized for the best phase contrast to 20 MHz as shown in Fig. 4j (see Supplementary Section E for the details). These results confirm that the thermophoretic force supports our phase detection via Eq. (1), as expected. This set of experiments support strong confirmations for the appearance of thermophoresis in our plasmonic gas sensing. Therefore, the sensitivity enhancement factor of 3,852 could be achieved by the association of plasmonic field enhancement, thermophoresis, and plasmonic optical trapping. More quantitative contribution of each phenomenon will be investigated in our future study.

The flow controller has technical limitation on the response speed and pressure amplitude, and thus cannot support the real-time detection test of single-molecule resolution fluid dynamics. Therefore, a new setup was designed using a speaker as a fast pressure modulator (see Fig. 5a). For different values of supplied voltage and applied frequency, the pressure change ($P_{dynamic}$) generated by sound waves in this experiment reached to 10 Pa (see Supplementary Table S5 – Section F). The controlled voltage was changed from 0 to 20 V with step size of 0.1 V, and the frequency was set below 500 Hz (phase

meter limitation). Gas flow with static pressure (P_{static}) (see Fig. 5a), which was controlled by the flow controller, passed through the speaker resulting in $P_{dynamic}+P_{static}$ at the outlet (see Methods for more detail). $P_{dynamic}$ was measured using two different techniques: the manometer principle and maximum bubble pressure methods for the calibration (see Supplementary Figure S3 – Section F). These two measurement results were comparable, therefore, the measured $P_{dynamic}$ was considered acceptable. For a frequency and supply voltages of 5 Hz and 20 V, $P_{dynamic}$ was 112.1 Pa, corresponding to a change in refractive index (Δn) of 2.8×10^{-7} (see Supplementary Table S6—Section F). The slope of the measured $P_{dynamic}$ with the supplied voltage was 10.3 Pa/V. Further, for the controlled frequency of 200 Hz, the measured pressure was 39.3 Pa corresponding to a Δn of 9.9×10^{-8} (see Supplementary Table S6—Section F).

To evaluate the resolution limit of the measurement method, Allan deviations were calculated at various averaging times (see Fig. 5f). The minimum stability was achieved at a sampling time of 0.2 s, corresponding to the frequency of 5 Hz. Therefore, 5 Hz was selected as the applied frequency to speaker in the high-resolution measurement. After performing the experiment, the phase at 5 Hz was resolved clearly in the Fourier transform data (see Fig. 5b). The maximum relative phase $\Delta\phi$, was 6.9. The relation between the relative phase and voltage is shown in Fig. 5c; the slope was of 0.35 $\Delta\phi$ *(rad)*/*V*. Combined with the relations between the pressure, voltage, refractive index, and number of gas atoms per hole in Supplementary Table S5—Section F, the relationship between the number of gas atoms per hole and relative phase was derived, as shown in Fig. 5d. The relation provided a slope of 319.6 atoms/hole/$\Delta\phi$ *(rad)*. The minimum controlled voltage step size was 0.1 V, indicating that a change of 11.2 atoms per hole ($\Delta n = 2.7 \times 10^{-9}$) was detected successfully. The measurement resolutions calculated by the Allan deviation were 0.12 atoms per hole ($\Delta n = 2.9 \times 10^{-11}$) (FCR non-differential plasmonic spectroscopy) and 0.06 molecule per hole ($\Delta n = 1.45 \times 10^{-11}$) (FCR differential plasmonic phase spectroscopy) (see Fig. 5f). Thus, the method can detect a change of one gaseous atom inside an area of 4×4 holes on the EOT sample surface.

To demonstrate the high-speed measurement of the refractive index using FCR plasmonic phase spectroscopy, a frequency of 200 Hz was applied to the speaker, which is the Nyquist frequency of the current phase meter with the sampling speed limited to 1 kHz. The phase data was processed and analyzed in the frequency domain and an expected peak of 200 Hz was observed (see Fig. 5e, left). Thus, to verify the signal caused by the pressure change on the sample surface or the vibration effect caused by the sound, the same experiment was conducted without the gas flow P_{static}. Consequently, the peak at 200 Hz disappeared (see Fig. 5e, right), which confirmed that the signal was because of the change in the refractive index.

We demonstrated that frequency-comb-referenced plasmonic phase spectroscopy enables fast and precise detection of gas dynamics via enhancing photon-sample interaction by 3852 times with the aids of plasmonic resonance and thermophoresis-assisted optical confinement around the nanoholes. As a demonstration, a small dynamic atom/molecule density modulation with an amplitude of 11.2 atoms per nanohole (2.7×10^{-9} in RIU) was clearly resolved at 5 Hz with a detection resolution of 0.06 atoms/nanohole (1.45×10^{-11} in RIU) in Allan deviation. The experimental results prove that the dynamic motions of gas density can be measured with an unprecedented single-molecule

resolution at a sampling rate of 200 Hz with the proposed scheme, which can enable real-time monitoring of fast gas dynamics. This fast and precise sensing technique can enable the in-depth analysis of fast fluid dynamics with the utmost resolution for better understanding of biomedical, chemical, and physical events and interactions. Functionalizing the plasmonic sample surfaces with selective bio-receptors, such as aptamers or bacteriophages, real-time detection of respiratory viruses could be realized without time-consuming PCR.

Methods

Frequency comb

The frequency comb used in our work is a spectrally broadened Er-doped fiber laser system (FC-1500–250-WG, M-VIS, Menlo Systems). The master oscillator is a mode-locked Er-doped fiber laser with a repetition rate (f_r) of 250 MHz, a center wavelength of 1,560 nm, and a spectral bandwidth of ~ 25 nm. The output is amplified using two Er-doped fiber amplifiers (EDFAs). One EDFA is used for frequency stabilization, where f_r and f_{CEO} are phase-locked to a reference Rb atomic clock (FS725, Stanford Research Systems) using an *f*-to-*2f* inte.

rferometer and phase-locked control loops. The other EDFA is used for nonlinear spectral broadening, where the amplified pulses are frequency-doubled to ~ 780 nm and then coupled into a photonic crystal fiber to generate a broad supercontinuum spanning from 530 to 950 nm.

The frequency comb is uniquely suited for our plasmonic phase spectroscopy technique due to its broad spectral coverage with narrow linewidths, absolute frequency referencing, and potential for multiplexed measurements. The wide spectrum allows simultaneous excitation of the plasmonic resonance and an off-resonance reference, which is crucial for differential phase detection. Locking the comb to an atomic clock provides a stable, absolute frequency reference for precise and repeatable phase measurements over extended timescales. Furthermore, the multiple comb lines open up future possibilities for probing the plasmonic response at several wavelengths simultaneously, enabling more comprehensive characterization of gas dynamics.

Mach–Zehnder interferometer

The frequency comb beam was split into two beams by an optical splitter. The first beam was the reference beam and had a frequency shift of 36.2 MHz due to the AOM. The second beam was transmitted through the gas chamber including the EOT sample. The two beams were recombined at the second beam splitter. They interfered and generated the heterodyne beat signal at the photodetector (PD). Using the appropriate grating-slit setup, two signals can be obtained at two different wavelengths. The measurement PD detected the beat at the plasmonic resonant (discussed in Fig. 2), which corresponded to the side slope in the phase spectrum, whereas the reference PD detected the beat off-resonance. When the refractive index of the material on the Au surface changes, the plasmonic condition is modified, which affects the phase of the measurement beat.

SPR resonance

At normal incidence, the SP wavelengths excited by the hole array are given approximately by Eq. 2. Because the metallic surface is in contact with two media (substrate glass and gas over the plasmonic structure), two groups of resonance can be observed [48].

$$\lambda_{max}(i,j) = \frac{a_0}{\sqrt{i^2+j^2}}\sqrt{\frac{\varepsilon_{S,L}\varepsilon_M}{\varepsilon_{S,L}+\varepsilon_M}} \tag{2}$$

where a_0 is the period of the array and ε_M, ε_S and ε_L are the dielectric constants of the metal, substrate and medium on the metal surface, respectively. i and j are the scattering orders of the array.

Pressure generator with speaker

The speaker was covered with a rubber membrane and a 5-mm thick acrylic film to make a pressure generator with two ports that acted as inlet and outlet. When a static pressure P_{static} was supplied, the rubber membrane was stretched and came into contact with the speaker diaphragm. The vibration of the speaker generates the vibration of gas inside the chamber, which was considered as dynamic pressure $P_{dynamic}$. By controlling the supplied voltage or frequency of the speaker, we can control the amplitude and rate of change of the $P_{dynamic}$. The entire set up was placed inside a metallic box with a wall thickness of 8 mm for sound isolation, which could affect the interferometer.

Thermophoresis analysis by FEM simulation

Electromagnetic and conjugate heat transfer problems can be solved using the commercial FEM solver (COMSOL Multiphysics). The "electromagnetics, beam envelopes" module was used to calculate the heat generated around the nanohole array. The entire simulation domain of the 20×20 nanohole array was reduced to a quarter by applying "PMC" and "PEC" boundary conditions along the x and y axes, respectively. Further, "Scattering" boundary conditions were used at the outer boundaries to prevent the reflection of the wave at the boundary, and "Matched" boundary conditions were used at the top and bottom to launch the Gaussian beam at 633 nm with a waist beam waist of 5 μm to the simulation domain. The compressible Navier–Stokes equation was solved by coupling the "Laminar Flow" module and the "Heat transfer in Solid/Fluid" module in the $400 \times 400 \times 400$ μm^3 domain. In the "Laminar Flow" module, "Inlet" and "Outlet" boundary conditions were set on the side for Argon flow into the simulation domain with a prescribed velocity and temperature: 0, 1, 5, and 10 μm/s at 293.15 K (see Supplementary Section G). No-slip boundary conditions and fixed temperature were set on all other boundaries. Then, gravitational body force was set to be ρ(T)g in the fluid domain. Temperature-dependent density data of Argon was taken from the COMSOL library. "Heat source" boundary conditions were applied on the volume of the nanohole array using the heat generation data exported from the electromagnetic simulation.

EOT chamber

EOT sample was covered with 1 mm thick slide glass. The gap between them was set by stacking two cover glass with a thickness of 150 μm. The epoxy was used to seal the chamber together with an inlet and outlet tube. The EOT sample used in our experiments has an area of 10 mm × 10 mm, covered with a thin layer of 100 nm gold. Within this sample, a square area of 1 mm^2 is engraved with evenly spaced holes to create an array that produces the extraordinary optical transmission (EOT) effect. Additionally, another square area on the same sample is scraped clean of the gold layer to serve as a reference.

FCR non-differential plasmonic spectroscopy

In this method, the beat frequency of the on-resonant 613-nm beam was compared with the radio frequency generated by the frequency generator. Because the frequency comb is tightly locked to a time standard, the phase noise caused by the light source is negligible in this investigation. However, the two interferometric arms are exposed to different disturbances of temperature, pressure, humidity, and CO_2 concentration, which cause time-dependent slow variations in the optical path difference (see Supplementary Figure S5a – Section H).

FCR differential plasmonic spectroscopy

In order to suppress the environmental noise, a differential phase detection method was implemented. The beat frequency of the on-resonant 613-nm beam was compared with the beat frequency of the off-resonant 780-nm beam (Fig. 2b, c). The wavelength-independent time-varying phase noise was efficiently cancelled. Because the reference signal traversed the same optical path as the measurement signal, the wavelength-independent common noise can be greatly suppressed. In addition, the concepts of common-path interferometry and balanced signal detection were implemented to provide higher noise immunity (see Supplementary Figure S5b – Section H).

Supplementary Information

The online version contains supplementary material available at https://doi.org/10.1186/s43074-024-00140-9.

Supplementary Material 1

Acknowledgements

This work was supported by the National Research Foundation of the Republic of Korea (NRF-2019K1A3A1A20092429, NRF-2020R1A2C2102338, NRF-2022M1A3C2069728 and RS-2024-00401786), and the Basic Research Program (NK236C) funded by the Korea Institute of Machinery and Materials (KIMM). This work was also supported by the KAIST UP Program and the Commercializations Promotion Agency for R&D Outcomes (COMPA) under grant RS-2023-00260002 and the Ministry of Small and Medium-sized Enterprises (SMEs) and Startups under grant RCMS-S3207602. We acknowledge the support of time and facilities from Ho Chi Minh City University of Technology (HCMUT), Viet Nam National University Ho Chi Minh City (VNU-HCM)

Author's contributions

The project was planned and overseen by S.K. and Y.-J.K. Plasmonic sample was designed, prepared and characterized by N.D.A., D.H.K., J.K.P, S.K. and H.J.C. Frequency-comb-referenced plasmonic spectroscopic experiments were performed by N.D.A., D.H.K., G.H.L., D.C.S and Y.-J.K. Data were analysed by N.D.A., G.H.L, and Y.-J.K. FEM simulation was performed by G.H.L. Frequency comb laser system was operated and monitored by D.C.S. and D.H.K. All authors contributed to the manuscript preparation.

Author information

Reprints and permissions information is available at www.nature.com/reprints. Correspondence and requests for materials should be addressed to S.K. (s.kim@pusan.ac.kr) and Y.-J.K. (yj.kim@kaist.ac.kr).

Availability of data and materials
The datasets used and/or analysed during the current study are available from the corresponding author on reasonable request. All data generated or analysed during this study are included in this published article (and its supplementary information files).

Declarations

Ethics approval and consent to participate
Not applicable.

Consent for publication
Not applicable.

Competing interests
Authors state no conflicts of interest.

Author details
[1]Department of Mechanical Engineering, Korea Advanced Institute of Science and Technology (KAIST), Science Town, Daejeon 34141, South Korea. [2]Department of Mechatronic Engineering, Faculty of Mechanical Engineering, Ho Chi Minh City University of Technology (HCMUT), Vietnam National University, Ho Chi Minh City, Vietnam. [3]Department of Cogno-Mechatronics Engineering, College of Nanoscience and Nanotechnology, Pusan National University, Busan 46241, South Korea. [4]Department of Optics and Mechatronics Engineering, College of Nanoscience and Nanotechnology, Pusan National University, Busan 46241, South Korea. [5]School of Mechanical and Aerospace Engineering, Nanyang Technological University (NTU), 50 Nanyang Avenue, Singapore 639798, Singapore. [6]Institute of Machinery and Materials, Nano-Convergence Mechanical Systems Research Division, Korea, 156, Gajeongbuk-Ro, Yuseong-Gu, Daejeon 34103, South Korea.

Received: 4 February 2024 Revised: 5 July 2024 Accepted: 29 July 2024
Published online: 13 August 2024

References

1. Alam MS, Karim F, Zhao C. Single-molecule detection at high concentrations with optical aperture nanoantennas. Nanoscale. 2016;8:9480–7.
2. Holzmeister P, Acuna GP, Grohmann D, Tinnefeld P. Breaking the concentration limit of optical single-molecule detection. Chem Soc Rev. 2014;43:1014–28.
3. Gooding JJ, Gaus K. Single-molecule sensors: Challenges and opportunities for quantitative analysis. Angew Chem Int Edit. 2016;55:11354–66.
4. Taylor AB, Zijlstra P. Single-molecule plasmon sensing: Current status and future prospects. Acs Sensors. 2017;2:1103–22.
5. Elson EL, Magde D. Fluorescence correlation spectroscopy I Conceptual basis and theory. Biopolymers. 1974;13:1–27.
6. Almehmadi LM, Curley SM, Tokranova NA, Tenenbaum SA, Lednev IK. Surface enhanced raman spectroscopy for single molecule protein detection. Sci Rep. 2019;9:12356.
7. Blackie EJ, Le Ru, E. C. & Etchegoin, P. G. Single-molecule surface-enhanced raman spectroscopy of nonresonant molecules. J Am Chem Soc. 2009;131:14466–72.
8. Nie SM, Emery SR. Probing single molecules and single nanoparticles by surface-enhanced raman scattering. Science. 1997;275:1102–6.
9. Lelek M, et al. Single-molecule localization microscopy. Nat Rev Methods Prim. 2021;1:39.
10. Pitschke M, Prior R, Haupt M, Riesner D. Detection of single amyloid β-protein aggregates in the cerebrospinal fluid of alzheimer's patients by fluorescence correlation spectroscopy. Nat Med. 1998;4:832–4.
11. Eid J, et al. Real-time DNA sequencing from single polymerase molecules. Science. 2009;323:133–8.
12. Rissin DM, et al. Single-molecule enzyme-linked immunosorbent assay detects serum proteins at subfemtomolar concentrations. Nat Biotechnol. 2010;28:595–9.
13. Bacia K, Kim SA, Schwille P. Fluorescence cross-correlation spectroscopy in living cells. Nat Methods. 2006;3:83–9.
14. Naz S, et al. Solid state gas sensor. Materials Today: Proceedings. 2022;49:3245–9.
15. Capone S, et al. Solid state gas sensors: state of the art and future activities. 2003;5:1335–48.
16. Dutta P, Horn PM. Low-frequency fluctuations in solids - 1-f noise. Rev Mod Phys. 1981;53:497–516.
17. Mühlschlegel P, Eisler HJ, Martin OJF, Hecht B, Pohl DW. Resonant optical antennas. Science. 2005;308:1607.
18. Novotny L, van Hulst N. Antennas for light. Nat Photonics. 2011;5:83.
19. Wientjes E, Renger J, Curto AG, Cogdell R, van Hulst NF. Strong antenna-enhanced fluorescence of a single light-harvesting complex shows photon antibunching. Nat Commun. 2014;5:4236.
20. Kinkhabwala A, et al. Large single-molecule fluorescence enhancements produced by a bowtie nanoantenna. Nat Photonics. 2009;3:654–7.
21. Fang Y, Seong NH, Dlott DD. Measurement of the distribution of site enhancements in surface-enhanced raman scattering. Science. 2008;321:388–92.
22. Gargiulo J, et al. Understanding and reducing photothermal forces for the fabrication of au nanoparticle dimers by optical printing. Nano Lett. 2017;17:5747–55.
23. Ashkin A. Acceleration and trapping of particles by radiation pressure. Phys Rev Lett. 1970;24:156–9.

24. Juan ML, Gordon R, Pang YJ, Eftekhari F, Quidant R. Self-induced back-action optical trapping of dielectric nanoparticles. Nat Phys. 2009;5:915–9.
25. Ashkin A, Dziedzic JM, Bjorkholm JE, Chu S. Observation of a single-beam gradient force optical trap for dielectric particles. Opt Lett. 1986;11:288–90.
26. Kotsifaki DG, Chormaic SN. Plasmonic optical tweezers based on nanostructures: fundamentals, advances and prospects. Nanophotonics. 2019;8:1227–45.
27. Hong C, Yang S, Ndukaife JC. Stand-off trapping and manipulation of sub-10 nm objects and biomolecules using opto-thermo-electrohydrodynamic tweezers. Nat Nanotechnol. 2020;15:908–13.
28. Anker JN, et al. Biosensing with plasmonic nanosensors. Nat Mater. 2008;7:442–53.
29. Willets KA, Van Duyne RP. Localized surface plasmon resonance spectroscopy and sensing. Annu Rev Phys Chem. 2007;58:267–97.
30. Schasfoort R & Tudos A. Handbook of surface plasmon resonance. 2007.
31. Jung LS, Campbell CT, Chinowsky TM, Mar MN, Yee SS. Quantitative interpretation of the response of surface plasmon resonance sensors to adsorbed films. Langmuir. 1998;14:5636–48.
32. Homola J. Surface plasmon resonance sensors for detection of chemical and biological species. Chem Rev. 2008;108:462–93.
33. Kabashin AV, Nikitin PI. Surface plasmon resonance interferometer for bio- and chemical-sensors. Optics Commun. 1998;150:5–8.
34. Kravets VG, et al. Singular phase nano-optics in plasmonic metamaterials for label-free single-molecule detection. Nat Mater. 2013;12:304.
35. Sreekanth KV, et al. Biosensing with the singular phase of an ultrathin metal-dielectric nanophotonic cavity. Nat Commun. 2018;9:369.
36. Anh ND, et al. Plasmonic dynamics measured with frequency-comb-referenced phase spectroscopy. Nat Phys. 2019;15:132–7.
37. Hansch TW. Nobel lecture: Passion for precision. Rev Mod Phys. 2006;78:1297–309.
38. Hall JL. Nobel lecture: Defining and measuring optical frequencies. Rev Mod Phys. 2006;78:1279–95.
39. Newbury NR. Searching for applications with a fine-tooth comb. Nat Photonics. 2011;5:186–8.
40. Steinmetz T, et al. Laser frequency combs for astronomical observations. Science. 2008;321:1335–7.
41. Predehl K, et al. A 920-kilometer optical fiber link for frequency metrology at the 19th decimal place. Science. 2012;336:441–4.
42. Lee J, Kim YJ, Lee K, Lee S, Kim SW. Time-of-flight measurement with femtosecond light pulses. Nat Photonics. 2010;4:716–20.
43. Rosenband T, et al. Frequency ratio of al+ and hg+ single-ion optical clocks; metrology at the 17th decimal place. Science. 2008;319:1808–12.
44. Geng XT, et al. Frequency comb transferred by surface plasmon resonance. Nat Commun. 2016;7:1–7.
45. Woo CH, Jang S, Shin G, Jung GY, Lee JW. Sensitive fluorescence detection of sars-cov-2 rna in clinical samples via one-pot isothermal ligation and transcription. Nat Biomed Eng. 2020;4:1168–79.
46. Tang Z, et al. A materials-science perspective on tackling covid-19. Nat Rev Mater. 2020;5:847–60.
47. Klompus S. et al. Cross-reactive antibodies against human coronaviruses and the animal coronavirome suggest diagnostics for future zoonotic spillovers. Sci Immunol 2021;6:eabe9950.
48. Krishnan A, et al. Evanescently coupled resonance in surface plasmon enhanced transmission. Optics Commun. 2001;200:1–7.
49. Grigorenko AN, Roberts NW, Dickinson MR, Zhang Y. Nanometric optical tweezers based on nanostructured substrates. Nat Photonics. 2008;2:365–70.
50. Jiang QB, Rogez B, Claude JB, Baffou G, Wenger J. Temperature measurement in plasmonic nanoapertures used for optical trapping. ACS Photonics. 2019;6:1763–73.
51. Garcia-Guirado J, et al. Overcoming diffusion-limited biosensing by electrothermoplasmonics. Acs Photonics. 2018;5:3673.
52. Roxworthy BJ, Bhuiya AM, Vanka SP, Toussaint KC. Understanding and controlling plasmon-induced convection. Nat Commun. 2014;5:3173.
53. Donner JS, Baffou G, McCloskey D, Quidant R. Plasmon-assisted optofluidics. ACS Nano. 2011;5:5457–62.
54. Braun M, Cichos F. Optically controlled thermophoretic trapping of single nano-objects. ACS Nano. 2013;7:11200–8.

Publisher's Note